



CuO–Fe₂O₃ nanoparticles embedded onto reduced graphene oxide nanosheets: a high-performance nanocomposite anode for Li-ion battery

Mohammad Ranjbar-Azad¹ · Mohsen Behpour^{1,2} · Fereshteh Keyhanian¹

Received: 2 April 2022 / Revised: 5 August 2022 / Accepted: 6 August 2022 / Published online: 20 August 2022
© The Author(s), under exclusive licence to Springer-Verlag GmbH Germany, part of Springer Nature 2022

Abstract

The development of safe, fast charging, and long-lasting Li-ion batteries has been taking major steps forward through novel combinations of nanomaterials. Here, using a co-precipitation technique, we embed CuO–Fe₂O₃ nanoparticles onto reduced graphene oxide (RGO) nanosheets for being employed as a Li-ion battery anode. The resultant CuO–Fe₂O₃/RGO nanocomposite (NC) shows an initial discharge capacity of 1339 mAh/g under a current density of 100 mA/g, together with coulombic efficiency of 84%. After 100 cycles, the respective discharge and charge capacities of the NC are found to be 859 and 850 mAh/g, indicating its high efficiency and durable cyclic performance. We also fabricate and characterize other RGO-based NCs such as CuO/RGO and Fe₂O₃/RGO in order to understand the improved electrochemical performance of the combined constituents.

Keywords RGO nanosheets · CuO–Fe₂O₃ nanoparticles · Nanocomposite · Cyclic stability · Cyclic voltammetry · Li-ion anode

Introduction

As the necessary tools to the world today, lithium (Li) batteries play important roles in a wide variety of devices such as mobile phones, laptops, tablets, electric vehicles, walking robots, drones [1–3]. For the past few years, the fabrication of high-energy batteries with durable cyclic performance has invigorated the scientific community to make them one step closer to practical applications [4, 5]. In this direction, designing miniature and lightweight batteries with high efficiency and long-term cycling stability for use as power sources in the next generation devices has presented challenges. These involve poor cyclability, low current efficiency, and short device longevity of the currently used materials for Li battery electrodes [6–8].

To improve electrochemical properties of the batteries, it is necessary to functionalize their different components, including the cathode electrode, electrolyte, separator, and anode electrode [9]. In this respect, new electrode materials have been introduced with the help of nanoscience. Among materials at the nanoscale, a large volumetric energy density and high theoretical capacity along with fast charge/discharge rates have been envisioned for transition-metal oxides (M_xO_y; where M represents the elements Fe, Cu, Ni, Ti, Co, Sn, etc.), outperforming the traditional graphite for Li-ion storage [10–16]. The large specific capacity, low cost, and high environmental benignity and availability of CuO and Fe₂O₃ compounds have made them ideal choices for use as efficient anode electrode materials [17–19]. Nevertheless, some flaws (e.g., low coulombic efficiency and rate performance) have been identified for these compounds due to their small conductivity for the lithiation/delithiation mechanism as well as their large volume expansion during the cycling process, thereby casting doubt on their utilization [20–22].

To eliminate these flaws, several approaches have been proposed in recent research studies. Notably, porous materials with hierarchical structures such as hollow spheres [23], core-shell [24], nanoflowers [25], pillar arrays [26], and

✉ Mohammad Ranjbar-Azad
m.ranjbarazad@gmail.com

¹ Institute of Nanoscience and Nanotechnology, University of Kashan, Kashan 87317-51167, Iran

² Department of Analytical Chemistry, Faculty of Chemistry, University of Kashan, Kashan 87317-51167, Iran

nanotubes [27] have been able to enhance electrochemical properties of the battery anodes because of their integrated functionality at the nanoscale.

Alternatively, nanocomposites (NCs) with hierarchical structures, comprising the transition-metal oxides and carbon materials, have been employed as efficient battery anodes by forming highly conductive network materials, while also avoiding the large volume expansions. Examples of such NCs are given as follows: hollow carbon spheres/reduced graphene oxide (RGO) [28], three-dimensional (3D) sandwich-structured NiMn_2O_4 @rGO [29], 3D-structured carbon-coated MnO/graphene [30], hollow C@MoS₂@PPy [31], Cu₂O/CuO/Cu/carbon-polymer composite fibers [32], α -Fe₂O₃@C [33], and hierarchical CuO@ MnO₂ core-shell nanosheet arrays [34]. In fact, the carbon contents of the NCs facilitate the network conductivity and improve the anode longevity and rate performance of the resultant batteries for the lithium storage. Among the carbon materials, RGO sheets have extremely large surface areas, which can in turn induce large electrical conductivity and high cycle stability in the NC structures [35, 36]. However, no reports could be found in the literature on the combination of RGO with the CuO–Fe₂O₃ compound in order to fabricate an RGO-based NC for being employed as the Li storage electrode.

In the present study, we fabricate CuO–Fe₂O₃/RGO NC for the Li anode material purposes using a facile chemical precipitation technique. We also characterize and investigate electrochemical properties of the resultant NC by evaluating the morphology, composition, crystal structure, Li storage capability, rate capability, and reversible capacity. To better understand the influence of the combined NC structure, we also fabricate and investigate the electrochemical properties of the constituent components separately (i.e., CuO/RGO and Fe₂O₃/RGO NCs). It is found that the electrochemical performance of the CuO–Fe₂O₃/RGO NC considerably outperforms that of other RGO-based NCs investigated in previous works.

Experimental details

Preparation of RGO nanosheets

All the chemicals and solvents (purchased from Merck) employed in this study were used without further purification. RGO nanosheets were prepared through a two-step synthesis technique. We initially oxidized and exfoliated natural graphite powders chemically by using an improved Hummers' method [37] and then carried out a chemical reduction process. In a typical synthesis, a quantity of 1 g of GO nanosheets was well dispersed in 200 ml of deionized water (DIW) under sonication for 30 min, and then 10 ml of hydrazine was added into it. The solution was magnetically

stirred for 12 h in an oil bath at 90 °C under a reflux condition. Ultimately, we filtered and rinsed the resulting solution, followed by drying the precipitate at room temperature (RT).

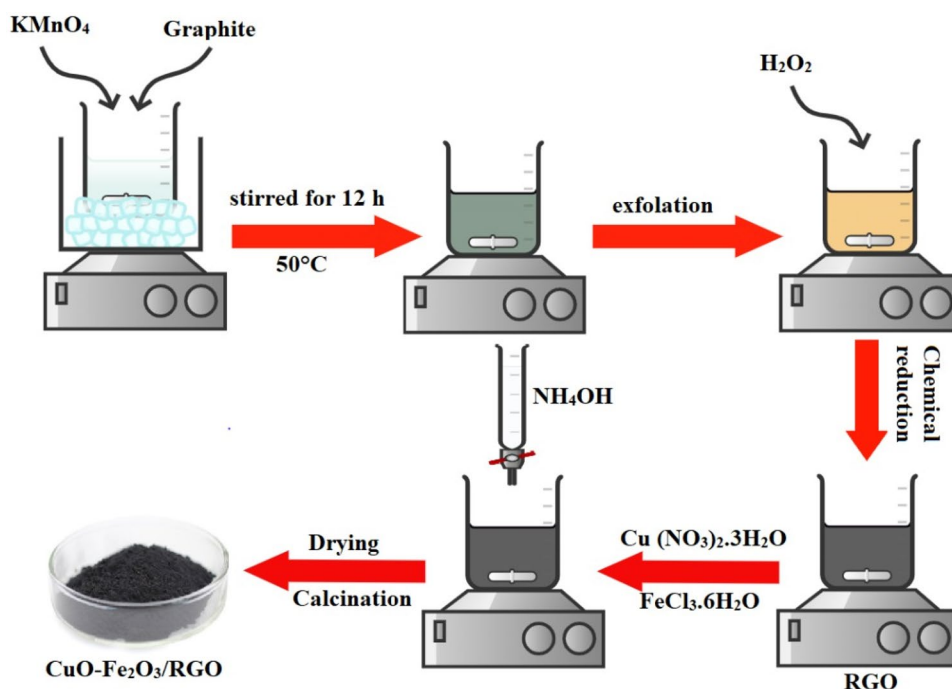
Preparation of RGO-based NCs

To prepare CuO/RGO NC, a co-precipitation technique was employed as described elsewhere [38]. For the fabrication of CuO–Fe₂O₃/RGO NC, an amount of 0.6 g of the CuO/RGO NC prepared previously was dispersed in 100 ml of DIW under sonication for 30 min; 1.4 g of FeCl₃·6H₂O was then added to the mixture and stirred at RT for 2 h. Ammonia solution (1 M) was added dropwise to the resulting solution (until the pH reached about 10), while also continuing the stirring at 80 °C for 1 h. The precipitate was filtered, rinsed with DIW, dried in an oven at 80 °C, and calcined at 500 °C for 2 h. For better clarity, Fig. 1 shows a schematic representation of the synthesis process of CuO–Fe₂O₃/RGO NC. It should be noted, in terms of electrochemical performance, the optimum molar ratio of CuO: Fe₂O₃ in the resulting CuO–Fe₂O₃/RGO NC was 1:1. We also fabricated the other RGO-based NC (Fe₂O₃/RGO) using the same conditions as described above, except adding the CuO/RGO powder to the solution.

Electrochemical characterization

We evaluated electrochemical properties of the RGO-based NCs (as anode materials) by assembling coin-type (CR-2032) testing cells with pure lithium foil, acting as both the counter and reference electrodes. The working electrode was fabricated by dispersing of the active material, carbon black (as the conductive agent), and polyvinylidene fluoride (as a binder) at a mass ratio of 8: 1: 1 in N-methyl-2-pyrrolidone solvent. We then coated the resulting slurry onto a thin Cu foil current collector and dried it at 120 °C overnight in a vacuum oven in order to remove the solvent. The electrodes were pressed and punched into circular disks with a diameter of 10 mm, followed by measuring the weight of their active materials. We finally assembled the cells in an Ar-filled glove box using a non-aqueous electrolyte, consisting of 1 M LiPF₆ dissolved in ethylene carbonate and diethyl carbonate (1:1 in vol%). A microporous polypropylene membrane was also employed as the separator. All cyclic voltammetry (CV) measurements were recorded using an Autolab electrochemistry workstation. In this regard, the voltage range and scanning rate were 0.01–3.0 V and 0.1 mV/s, respectively. Electrochemical impedance spectroscopy was examined over a frequency range from 100 kHz to 0.01 Hz by applying an AC voltage of 5 mV. At RT, galvanostatic discharge/charge tests were carried out on a battery tester (NEWARE) for different current densities (ranging from 0.1 to 1 A/g).

Fig. 1 The schematic representation of the synthesis process of CuO–Fe₂O₃/RGO NC



Instrumentation

The crystalline properties of RGO nanosheets and RGO-based NCs were evaluated on a Philips-X'pert Pro X-ray diffractometer (XRD, $\text{Cu-K}\alpha$ radiation, $\lambda = 0.15418 \text{ \AA}$) in the 2θ range from 10 to 80° at RT. Fourier transform infrared (FTIR) spectroscopy was examined on a Nicolet Magna-550 spectrophotometer using the KBr pellet method in the range of $400\text{--}4000 \text{ cm}^{-1}$. Raman spectroscopy was recorded using a micro-Raman spectrometer (TakRam N1-541-Teksan) equipped with excitation of the 1064-nm line. The specific surface area and porosity of the NCs were determined by N_2 adsorption using Brunauer–Emmett–Teller (BET, Belsorp mini II, Microtrac Bel Corp) method. The morphology of the RGO nanosheets and RGO-based NCs was characterized using field-emission scanning electron microscopy (FESEM, ZEISS SUPRA 40VP, Germany) and transmission electron microscopy (TEM, Philips, CM120, Netherlands). Typically, elemental analysis was evaluated with an energy-dispersive X-ray (EDX, VEGA\TESCAN-XMU) mapping spectroscopy.

Results and discussion

Structural, morphological, and compositional results

The crystal phase of the as-prepared RGO nanosheets and RGO-based NCs was investigated by XRD analysis, and

the results are illustrated in Fig. 2. According to the XRD pattern of RGO, two broader peaks ($2\theta \sim 24.9^\circ$ and 45.5°) appear, which can be indexed to (002) and (100) planes. The lattice spacing of 0.36 nm is also obtained, indicating the elimination of most of the oxygen functional groups during the chemical reduction [39]. The diffraction pattern of the CuO/RGO NC could be indexed to the monoclinic phase of CuO (JCPDS, card no. 80–1916), having two intensive peaks centered at $2\theta \sim 35.7^\circ$ and 38.8° corresponding to (-111) and (111) planes, respectively. The typical diffraction peaks revealed in the XRD pattern of $\text{Fe}_2\text{O}_3/\text{RGO}$ NC at $2\theta = 34.3^\circ$

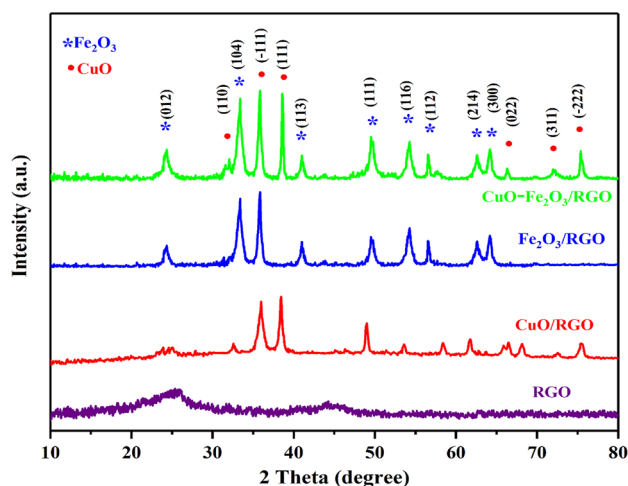


Fig. 2 XRD patterns of as-prepared RGO nanosheets and RGO-based NCs

and 36.1° can be related to (104) and (110) planes, respectively, confirming the formation of the hexagonal structure of $\alpha\text{-Fe}_2\text{O}_3$.

In the case of $\text{CuO-Fe}_2\text{O}_3/\text{RGO}$ NC, all the observed peaks confirm the formation of both the hexagonal structure of $\alpha\text{-Fe}_2\text{O}_3$ and monoclinic structure of CuO . Note that, for all the RGO-based NCs, the appearance of (002) diffraction peak around $2\theta = 25^\circ$ can be attributed to RGO nanosheets with less agglomeration. Also, the absence of impurity peaks evidences that the resultant NCs are pure and have high quality. To evaluate crystallite size of the NCs, we used Scherrer's formula as follows:

$$\tau = \frac{K\lambda}{\beta \cos \theta} \quad (1)$$

where τ is the crystallite size value, β is the full width at half maximum of the peak, K is the shape factor ($K=0.94$), θ is the diffraction angle (in radians), and λ is the wavelength of the X-ray ($\lambda=0.154$ nm). In this respect, the crystallite sizes were obtained to be about 38 nm, 32 nm, and 35 nm for CuO , Fe_2O_3 , and $\text{CuO-Fe}_2\text{O}_3$ nanoparticles, respectively. It appears that the crystallite size of the $\text{CuO-Fe}_2\text{O}_3$ nanoparticles is equal to the average value of the crystallite sizes of CuO and Fe_2O_3 nanoparticles, indicating the formation of uniform NC.

Figure 3 shows Raman spectra of the RGO nanosheets and RGO-based NCs. The two peaks appearing around ~ 1365 and ~ 1592 cm^{-1} are attributable to D and G bands of the disordered and graphitic carbon, respectively, being consistent with previous observations [40]. The G band can be ascribed to the E_{2g} mode in the basal plane of sp^2 carbon atoms, which in fact indicates the existence of highly ordered pyrolytic graphite. Alternatively, the D band can be associated with disordered hybridization and lack of long-range order in carbon atoms with amorphous and quasi-crystalline

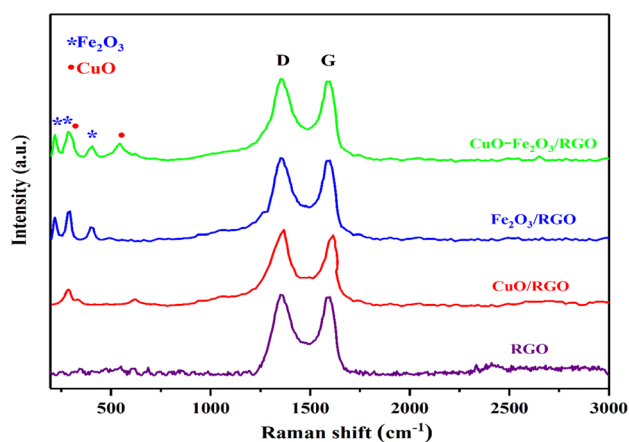


Fig. 3 Raman spectra of RGO nanosheets and RGO-based NCs

structures. For the CuO/RGO NC, the Raman spectrum shows a peak in the 283 cm^{-1} regions, corresponding to the A_g mode. Moreover, the induced dipole moment is located along the b -axis. The peaks in the 325 and 615 cm^{-1} regions are related to the B_g mode (being perpendicular to it), which can be associated to the monoclinic structure of CuO . Also, we see peaks of the Fe-O stretching vibration located around 220 cm^{-1} in the Raman spectrum of $\text{Fe}_2\text{O}_3/\text{RGO}$ NC, corresponding to the A_{1g} mode. The peaks at 293 and 399 cm^{-1} arise from the E_g mode, indicating the successful fabrication of the $\text{Fe}_2\text{O}_3/\text{RGO}$ NC. The Raman spectrum of $\text{CuO-Fe}_2\text{O}_3/\text{RGO}$ NC indicates peaks in the same or close wavenumbers to the ones stated in the Raman spectra of CuO/RGO and $\text{Fe}_2\text{O}_3/\text{RGO}$ NCs. However, we also observe slight shifts of the Raman peaks when both oxides are present in the NC, likely arising from surface strain changes and the presence of defects induced by the interaction between CuO and Fe_2O_3 phases in the NC structure [41].

As a complementary technique to Raman spectroscopy, we used FTIR spectroscopy in order to study the type of functional groups of the RGO nanosheets and RGO-based NCs, and the results are given in Fig. 4. We can clearly observe typical adsorption signals for all the compounds, comprising the wide band in the 3430 cm^{-1} region (belonging to the O-H stretching vibration of carboxyl groups) and intense bands centered at 1395 and 1115 cm^{-1} (being attributable to C=O antisymmetric bridge stretching vibration of the carbonyl or carboxyl groups and the epoxy groups, respectively). In the case of $\text{Fe}_2\text{O}_3/\text{RGO}$ NC, the broad peak in the 575 cm^{-1} region is related to the stretching vibration of the Fe-O bond in the NC structure, and the characteristic peak at 1625 cm^{-1} is indicative of the vibration of hydroxyl groups on the surface of Fe_2O_3 nanoparticles. The FTIR

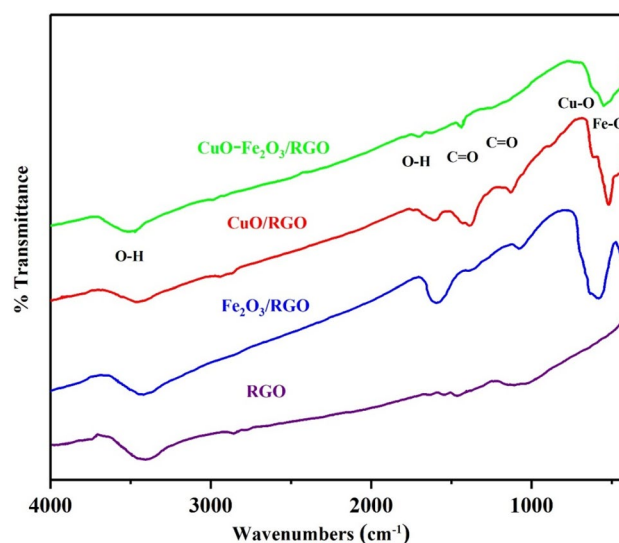


Fig. 4 FTIR spectra of RGO nanosheets and RGO-based NCs

spectrum of the CuO–Fe₂O₃/RGO NC reveals the characteristic peak in the 525 cm⁻¹ regions, and the appearance of two weak peaks around 475 and 610 cm⁻¹, which can be attributed to the presence of Fe–O bands and vibrations of the Cu–O bonds in the CuO structure. Note that the intensity of the vibration of hydroxyl groups of CuO–Fe₂O₃/RGO NC decreases due to interaction between CuO and Fe₂O₃.

The specific surface area and porous structure of the RGO-based NCs were determined by N₂ adsorption–desorption isotherms, and the results obtained are depicted in Fig. 5. From Fig. 5a, the three isotherms exhibit characteristic type II and type IV isotherms, together with obvious hysteresis loops which indicate the existence of macropores (> 50 nm) and mesopores (2–50 nm). The existence of macropores can be related to the stacked layer structure of RGO in the NC [42]. It is found that CuO/RGO, Fe₂O₃/RGO, and CuO–Fe₂O₃/RGO NCs possess specific surface areas of 117.28, 123.25, and 127.39 m²/g, respectively. Additionally, the pore size distribution curves of the RGO-based NCs are shown in Fig. 5b, which further confirm the existence of the mesoporous structure. As inferred, the average pore diameters of CuO–Fe₂O₃/RGO, Fe₂O₃/RGO, and CuO/RGO NCs mainly are found to be 6.4, 4.7, and 5.4 nm, respectively. Accordingly, the formation of mesoporous structure with high specific surface area provides fast ion diffusion pathways and improves electronic/ionic conductivity of the composite [43].

The surface morphology and particle size of RGO nanosheets and RGO-based NCs were investigated by FESEM and TEM experiments, and the corresponding images are depicted in

Fig. 6. From Fig. 6a, RGO nanosheets form 2D multilayers with randomly distributed structure, having relatively large surfaces with folded edges. In Fig. 6b–d, FESEM images show that nanoparticles formed in the NC structure have spherical-like morphology with approximately uniform sizes, decorating the surface of the RGO nanosheets. The respective mean particle sizes of CuO, Fe₂O₃, and CuO–Fe₂O₃ nanoparticles, evaluated from the FESEM images using Digimizer software, are found to be about 50, 43 and 45 nm. Figure 6e, f shows TEM images obtained from the CuO–Fe₂O₃/RGO NC. As can be seen, the CuO–Fe₂O₃ nanoparticles located on the transparent sheets of RGO form a sandwich-like structure.

On the other hand, SEM–EDX color mapping was carried out to characterize elemental composition of the CuO–Fe₂O₃/RGO NC, and the results are presented in Fig. 7. As observed, the elemental mapping results indicate that the elements C, O, Cu, and Fe are uniformly distributed on the RGO nanosheets.

Electrochemical characteristics

We investigated electrochemical performance of the RGO-based NCs by employing the Li sheet as both counter and reference electrodes. We initially assessed the Li-ion storage behavior using CV curves with a voltage range of 0.01–3 V and a scan rate of 0.1 mV/s, as can be seen in Fig. 8. From Fig. 8a, we observe three cathodic peaks at 1.9, 1, and 0.7 V (vs Li⁺/Li) during the first discharge process. The first two peaks correspond to the multistep reversible electrochemical reaction, forming an intermediate solid solution (induced

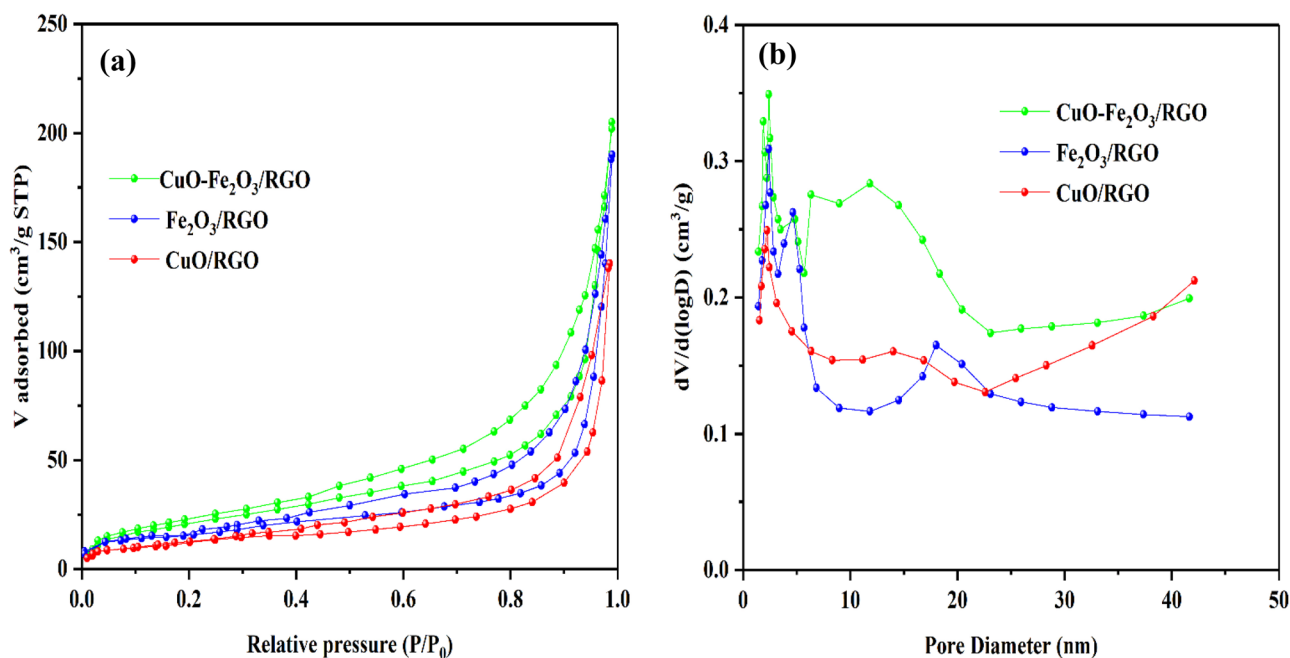


Fig. 5 (a) N₂ adsorption–desorption isotherms and (b) pore size distributions of RGO-based NCs

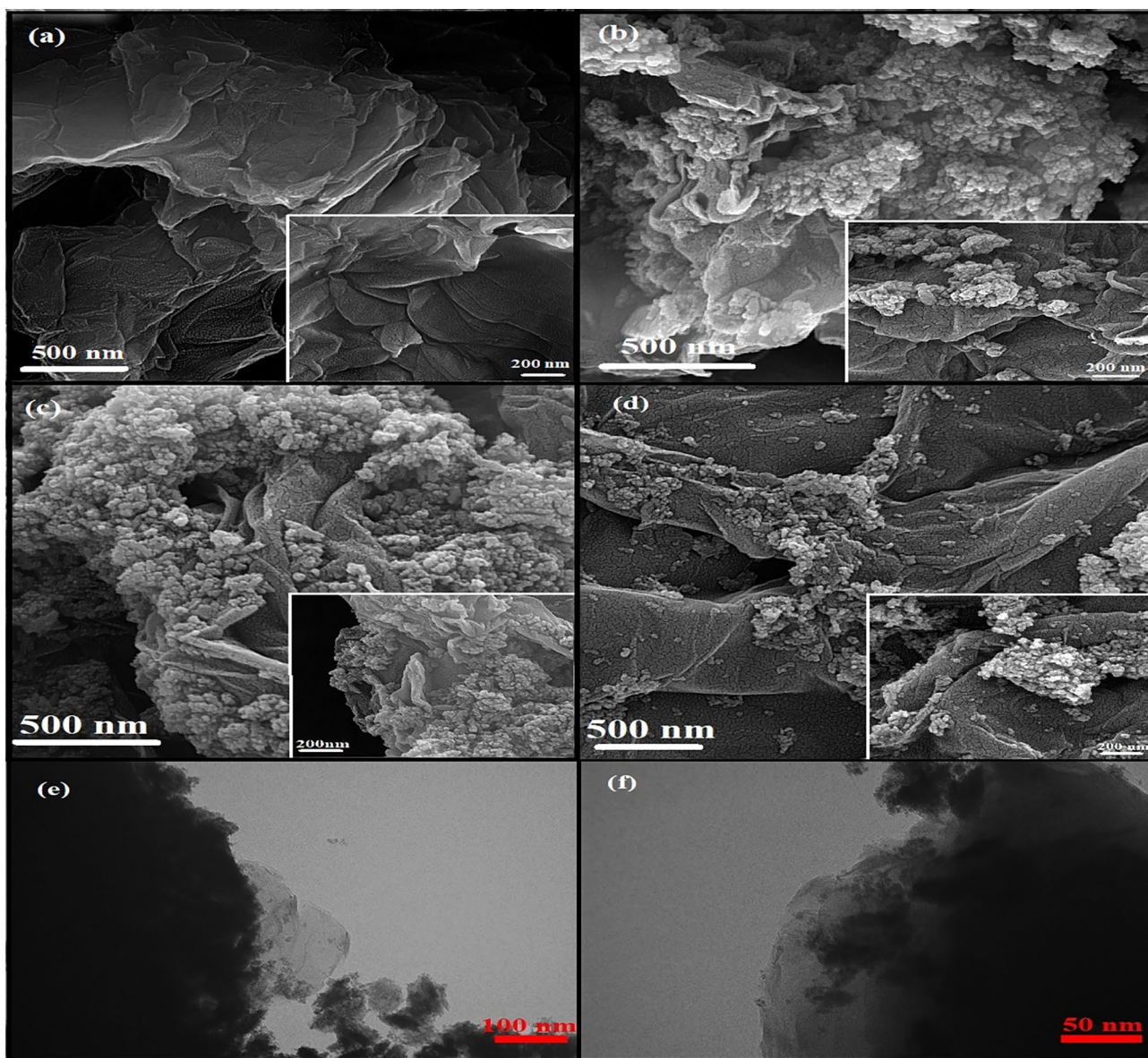
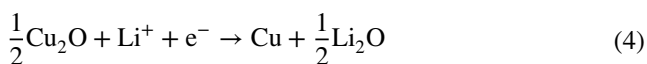
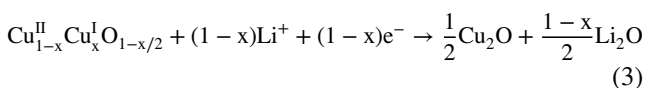
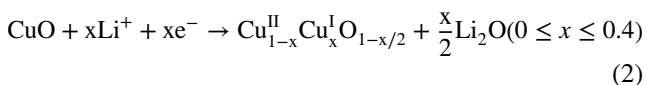


Fig. 6 FESEM images of RGO nanosheets and RGO-based NCs: (a) RGO nanosheets, (b) CuO/RGO NC, (c) Fe₂O₃/RGO NC, and (d) CuO–Fe₂O₃/RGO NC. The insets in panels (a)–(d) show the corre-

sponding high magnification images. (e) and (f) TEM images of the CuO–Fe₂O₃/RGO NC

by the intercalation of Li-ions in the CuO phase) and Cu₂O phase. The third peak results from the further decomposition of Cu₂O into metallic Cu and amorphous Li₂O phases due to the conversion reaction. These observations are in well agreement with previous reports [10]. One can express the reactions involved in the discharge process as follows [44]:



Additionally, we see three anodic peaks at the voltages of 1.5 V and 2.5 V and 2.7 V during the anodic scan of the CuO/RGO NC electrode. The first two peaks may arise from the partial decomposition of the solid-electrolyte interphase layer and the re-oxidation of the metallic phase of Cu to Cu₂O. We ascribe the third peak to the re-oxidation of the metallic phase of Cu to CuO. Note that the 2nd and 3rd CV curves nearly overlap with each other, making the electrode be highly reversible.

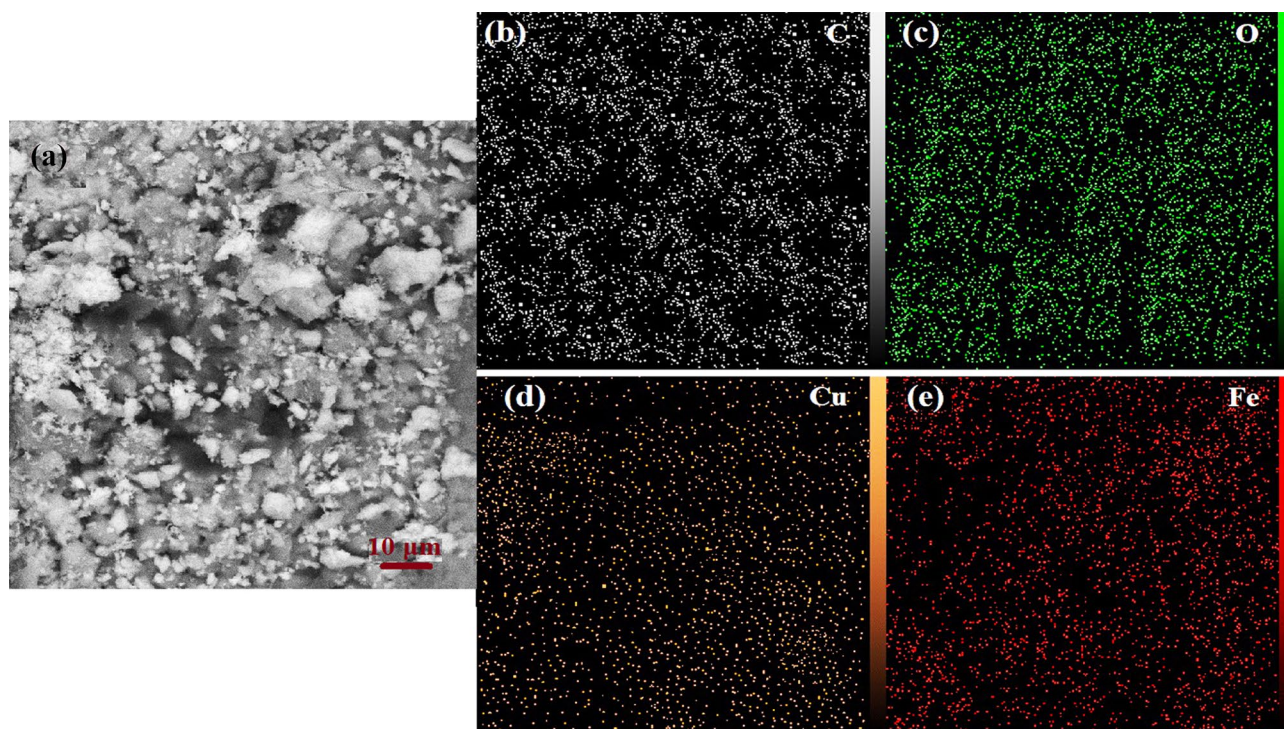
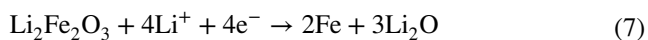
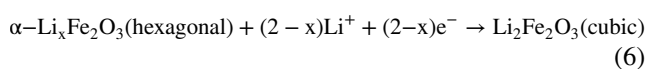
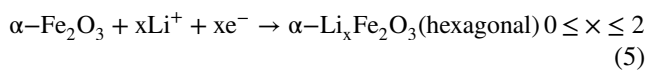


Fig. 7 SEM–EDX color mapping of the CuO–Fe₂O₃/RGO NC: (a) SEM image; and elements: (b) C, (c) O, (d) Cu, and (e) Fe

From Fig. 8b, we observe two well-defined reduction peaks in the first discharge process of the Fe₂O₃/RGO NC electrode, corresponding to the different reaction stages. The minor reduction peak appearing around 1.5 V may be caused by the initial Li-ion insertion into the Fe₂O₃ structure, thereby forming Li_xFe₂O₃ without changing the structure. As well, formation of an irreversible solid-electrolyte interphase film on the surface of the active materials is indicated.

The strong cathodic peak at 0.7 V is due to the phase change from hexagonal α-Li_xFe₂O₃ to cubic Li₂Fe₂O₃, followed by the complete reduction to Fe⁰ with further formation of Li₂O. The relevant reaction mechanism is given below [45]:



In the subsequent cycles, owing to the irreversible phase transformation in the first cycle, the main peak intensity is reduced perceptibly, and a positive shift of the peaks to a higher voltage of 1 V is observed. On the other hand, during the first anodic sweep, the two broad overlapped anodic peaks are noticeable at voltages of approximately 1.75 and 2 V, being assignable to the decomposition of the

solid-electrolyte interphase layer, the reversible multistep oxidation of Fe to FeO, and further oxidation to Fe₂O₃ accompanied with the Li-ion extraction. During the following cycles, these features do not shift, although they gradually merge with each other. The voltage–current curves are nearly overlapping during the following two cycles. This is indicative of the redox reactions with high reversibility, which is later confirmed by the cycling performance.

According to Fig. 8c, the CV profiles of the CuO–Fe₂O₃/RGO NC electrode display two pairs of peaks. During the 1st cathodic cycle, we observe a small peak around 1.6 V, relating to the structural transition induced by insertion of Li ions into the CuO–Fe₂O₃ structure. In addition, the intense cathodic peak centered at 0.5 V is attributable to further transformation of the Li_xFe₂O₃/Li_xCuO to the Fe^{II}/Cu^I, being accompanied with the further reduction into both of the Fe and Cu metals and the Fe–Cu alloy in the Li₂O matrix. The movement of the first reduction peaks in the subsequent cycles may result from the formation of the solid-electrolyte interphase layer and from the structural modification of Li-ion transfer mechanism during the lithiation process.

In the subsequent charge process, we observe a broad anodic peak in the voltage range of 1.5–1.9 V. One can ascribe this peak to the reversible multistep oxidation of Fe/Cu to Li_xFe₂O₃/Li_xCuO and then to Fe^{II}/Cu^I. The peak located around the voltage of 2.3 V represents the oxidation of Fe^{II}/Cu^I to Fe^{III}/Cu^{II} after being converted back to

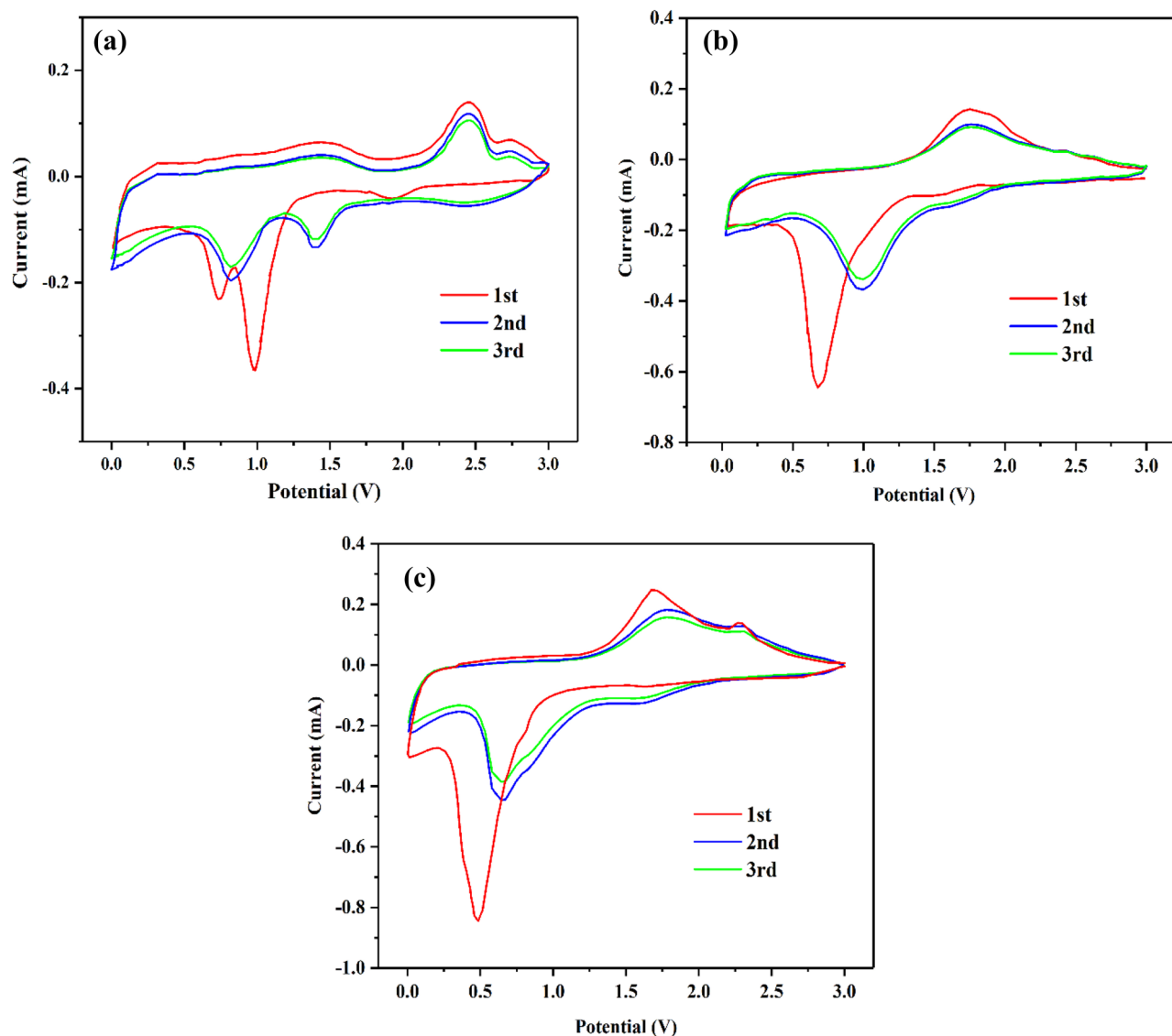


Fig. 8 CV curves of RGO-based NC electrodes: (a) CuO/RGO, (b) Fe₂O₃/RGO, and (c) CuO–Fe₂O₃/RGO

nanograins of CuO–Fe₂O₃ with the decomposition of Li₂O [46]. Furthermore, high reversibility of the electrochemical reactions and good stability of the CuO–Fe₂O₃/RGO NC electrode are indicated by the nearly overlapped 2nd and 3rd CV curves.

The discharge/charge voltage-capacity profiles of the RGO-based NC electrodes obtained from the initial three cycles at a specific current density of 100 mA/g and the voltage range of 0.02–3.0 V (vs. Li/Li⁺) are shown in Fig. 9. For the CuO/RGO NC electrode, we observe two flat discharge plateaus around 1.1–1.5 and 0.5–1 V (see Fig. 8a), corresponding to the reduction of Fe₂O₃/CuO to Fe/Cu alloy along with the formation of Li₂O and solid-electrolyte interphase layer. In addition, during the charge curve, one voltage plateau is found to be located at 2.6 V, being in

well agreement with the voltage peaks observed in the CV curves. During the initial charge/discharge curves, the electrode delivers a specific discharge capacity of 790 mAh/g and a subsequent charge capacity of 650 mAh/g, giving rise to initial coulombic efficiency of 82.0%. The considerable initial capacity loss is most likely due to the irreversible formation of a solid-electrolyte interphase layer and the incomplete conversion reaction. This behavior is common for most anode materials [47].

It can be seen in the first discharge curve of the Fe₂O₃/RGO NC electrode that only a broad voltage plateau occurs at ~0.75 V in conjunction with an inclined profile down to a cutoff voltage of 0.01 V. This is likely assignable to the reduction of Fe^{III} to Fe, the solid-electrolyte interphase layer formation, and the decomposition of the electrolyte. Also, the charge

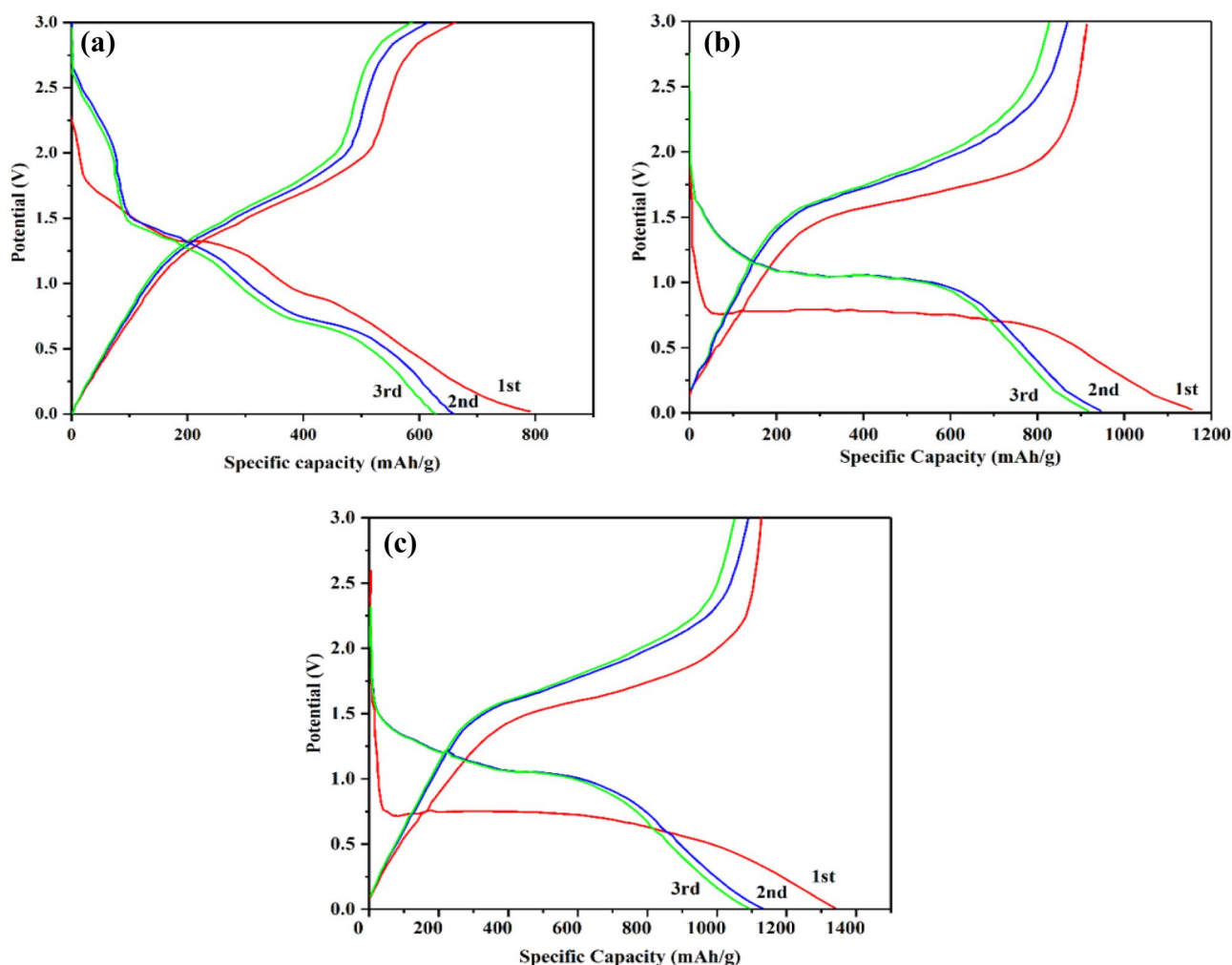


Fig. 9 Discharge/charge curves of RGO-based NC electrodes: (a) CuO/RGO, (b) Fe₂O₃/RGO, and (c) CuO–Fe₂O₃/RGO

curves show a sloped voltage plateau in the range of 1.5–2 V, being in accordance with the results of the CV measurements.

We observe that the Fe₂O₃/RGO NC anode (Fig. 9b) exhibits a lithium storage capacity of 1154 mAh/g during the initial discharge process. Nevertheless, a relatively low reversible capacity (913 mAh/g) is found for this electrode, leading to initial coulombic efficiency of 80%. We ascribe the relatively low initial coulombic efficiency to the inevitable formation of the solid-electrolyte interphase and decomposition of organic electrolytes, being common to most anode materials. Similarly, in the voltage profile of the CuO–Fe₂O₃/RGO NC anode, the initial discharge process comprises a flat voltage plateau at 0.75 V, replacing the sloped plateau in the voltage range between 1.5 and 1 V. The charge curves show a sloped plateau in the voltage range between 1.6 and 2.3 V (see Fig. 8c), which accord with the CV results [48]. The first three charge/discharge capacities of the CuO–Fe₂O₃/RGO NC anode are obtained to be approximately 1339/1127, 1131/1091,

and 1093/1049 mAh/g, respectively, together with initial coulombic efficiency of 84%.

Figure 10a shows the cycling performance of the three RGO-based NC anodes during cycling at a current density of 100 mA/g. The CuO–Fe₂O₃/RGO NC has the best cyclic stability and retention capacity among the anode materials when increasing the number of cycles. After 100 cycles, the reversible discharge/charge capacity of CuO–Fe₂O₃/RGO, Fe₂O₃/RGO, and CuO/RGO NCs tends to be stable, maintaining at 859/850, 717/701, and 467/457 mAh/g, respectively. The rate performance of the NCs was also tested at various current rates ranging from 0.1 to 1.0 A/g and then back to 0.1 A/g. Based on Fig. 10b, the CuO–Fe₂O₃/RGO NC displays average specific capacities of 1083, 905, 781, and 609 mAh/g at cycling rates of 0.1, 0.2, 0.5, and 1 mA/h, respectively.

In this way, by combining RGO nanosheets and CuO–Fe₂O₃ nanoparticles, one can acquire appropriate Li storage properties with reversible specific capacities compared to the other

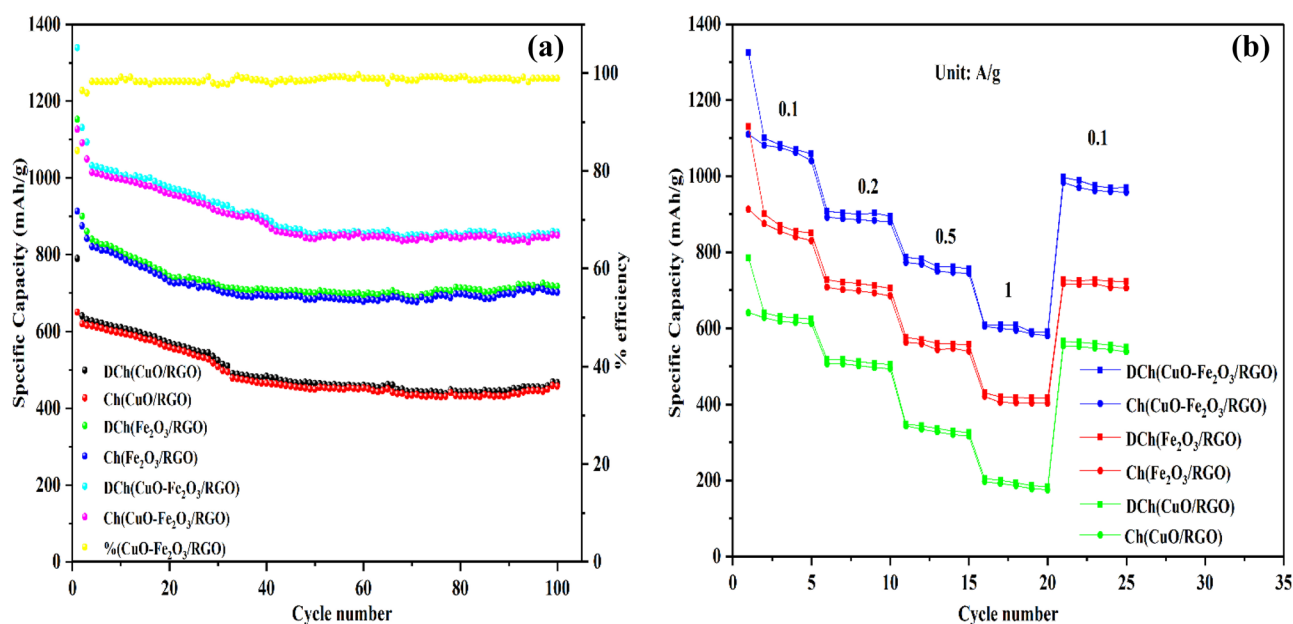


Fig. 10 (a) Cyclic performances of the RGO-based NCs along with coulombic efficiency of the CuO–Fe₂O₃/RGO NC at a current rate of 0.1 A/g. (b) The comparison between rate capabilities of the NCs at different current rates (0.1–1.0 A/g)

RGO-based NCs. The suppression of pulverization and low volume expansion of the CuO–Fe₂O₃ nanoparticles during long-term cycles may be responsible for the enhanced storage properties.

Li storage performance of the CuO–Fe₂O₃/RGO NC and related Fe₂O₃/C anode materials reported in the literature is compared with each other in Table 1. As can be inferred, the anode NC investigated in this work for Li-ion battery possesses higher capacity than most of the reported anodes after cycling, likely owing to the combination of the highly conductive RGO nanosheets with the transition-metal oxide CuO–Fe₂O₃ nanoparticles.

We performed electrochemical impedance spectroscopic measurements to investigate the electrochemical reaction features, kinetics, and diffusion of the RGO-based NC electrodes

in detail. These measurements were carried out at an open-circuit voltage and frequency range of 100 kHz–0.01 Hz. Figure 11 shows the Nyquist plots obtained from the RGO-based NCs, comprising a semicircle in the high-frequency range referring to the SEI layer resistance (R_{SEI}), dielectric relaxation capacitance (CPE_{SEI}), a semicircle in the medium frequency region associated with the charge transfer resistance (R_{ct}), and double-layer capacitance ($CPE_{electrode}$) induced between the electrode/electrolyte interface. A sloping straight line is also observed in the low-frequency region, demonstrating the Warburg impedance (Z_w). This can be attributed to the mass transfer of lithium ions within the solid electrode material [56]. The inset shows the corresponding equivalent circuit model. We find that R_{ct} of the CuO–Fe₂O₃/RGO NC is about 81.8 Ω , being substantially inferior to that of the

Table 1 Electrochemical performance of different Fe₂O₃-based materials for Li-ion battery anodes reported in the literature and this work. Note: The electrolytes of the comparing nanocomposite are the same

Material	Current density (mA/g)	Reversible capacity/cycle (mAh/g)	Initial discharge/charge capacity (mAh/g)	Ref
Fe ₂ O ₃ /graphene composite	100	708/300	1350/890	[49]
Fe ₂ O ₃ /graphene aerogel	93	875/50	1254/995	[50]
rGO/Fe ₂ O ₃ composite	100	1007/100	1468/1251	[51]
Carbon-coated α -Fe ₂ O ₃ @Fe ₃ O ₄	100	721/100	1697/1203	[52]
NiFe ₂ O ₄ /NiO@Fe ₂ O ₃ core-shelled nanocubes	500	832/150	—	[53]
Fe ₂ O ₃ /porous gC ₃ N ₄ /graphene	50	980/50	1282/—	[54]
3D net-like FeO _x /C	200	851/50	1204/854	[55]
CuO–Fe ₂ O ₃ /RGO NC	100	859/100	1339/1127	This work

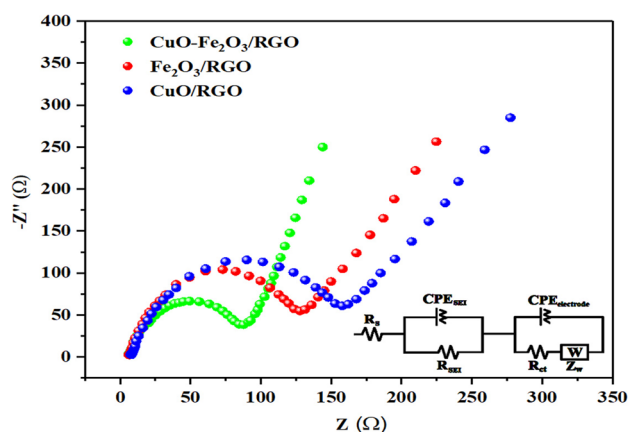


Fig. 11 Nyquist plots of RGO-based NC electrodes. The inset shows the corresponding equivalent circuit model

CuO/RGO ($R_{ct} = 151.9 \Omega$) and the $\text{Fe}_2\text{O}_3/\text{RGO}$ ($R_{ct} = 121.9 \Omega$) NCs. Therefore, we can state that the specific structure of the CuO– $\text{Fe}_2\text{O}_3/\text{RGO}$ NC (employed as an anode material) has more space to adapt to the change of volume, while also promoting the lowest diffusion of Li-ion and rapid charge transport during the electrochemical lithiation/delithiation processes.

Conclusion

We have fabricated RGO nanosheets and RGO-based NCs, including CuO/RGO, $\text{Fe}_2\text{O}_3/\text{RGO}$, and CuO– $\text{Fe}_2\text{O}_3/\text{RGO}$, and characterized their structural, morphological, compositional, and electrochemical property by different techniques. The CuO, Fe_2O_3 , and CuO– Fe_2O_3 nanoparticles were fine in size (≤ 50 nm) and uniformly distributed on the 2D nanosheets as indicated by XRD, FESEM, TEM, and SEM–EDX investigations. These spherical-like nanoparticles, in particular CuO– Fe_2O_3 ones, could provide large active surfaces with enhanced acceleration of redox reactions involved in the lithiation/delithiation mechanism. The CV experimented showed that the discharge/charge capacity of the CuO– $\text{Fe}_2\text{O}_3/\text{RGO}$ NC was considerably higher than that of the other RGO-based NCs after the 1st (1339/1127 mAh/g) and 100th cycles (859/850 mAh/g) when assembled in a Li-ion battery. These improved electrochemical properties were attributed to efficient combination of the highly conductive RGO nanosheets with the transition-metal oxide CuO– Fe_2O_3 nanoparticles.

Data availability The data will be available upon request.

Code availability Not applicable.

Declarations

Consent for publication By submitting the manuscript, the authors understand that the material presented in this manuscript has not been published before, nor has it been submitted for publication to another journal. The corresponding author attests that this study has been approved by all the co-authors concerned.

Conflict of interest The authors declare no competing interests.

References

- Shiyou Z, Fei D, Yuepeng P, Pan H, Junhe Y (2020) Research progress on nanostructured metal oxides as anode materials for Li-ion battery. *J Inorg Mater* 35(12):1295
- Yang Y, Yuan W, Kang W, Ye Y, Pan Q, Zhang X, Tang Y (2020) A review on silicon nanowire-based anodes for next-generation high-performance lithium-ion batteries from a material-based perspective. *Sustain Energy Fuels* 4(4):1577–1594
- Ai W, Luo Z, Jiang J, Zhu J, Du Z, Fan Z, Yu T (2014) Nitrogen and sulfur codoped graphene: multifunctional electrode materials for high-performance Li-ion batteries and oxygen reduction reaction. *Adv Mater* 26(35):6186–6192
- Etacheri V, Marom R, Elazari R, Salitra G, Aurbach D (2011) Challenges in the development of advanced Li-ion batteries: a review. *Energy Environ Sci* 4(9):3243–3262
- Kim T, Park J, Chang S, Choi S, Ryu J, Song H (2012) The current move of lithium-ion batteries towards the next phase. *Adv Energy Mater* 2(7):860–872
- Li H, Yu H, Zhang X, Guo G, Hu J, Dong A, Yang D (2016) Bowl-like 3C-SiC nanoshells encapsulated in hollow graphitic carbon spheres for high-rate lithium-ion batteries. *Chem Mater* 28(4):1179–1186
- Shin J, Samuelis D, Maier J (2011) Sustained lithium-storage performance of hierarchical, nanoporous anatase TiO_2 at high rates: emphasis on interfacial storage phenomena. *Adv Funct Mater* 21(18):3464–3472
- Laruelle S, Grugeon S, Poizot P, Dolle M, Dupont L, Tarascon J (2002) On the origin of the extra electrochemical capacity displayed by MO/Li cells at low potential. *J Electrochem Soc* 149(5):A627
- Nayak P, Yang L, Brehm W, Adelhelm P (2018) From lithium-ion to sodium-ion batteries: advantages, challenges, and surprises. *Angew Chem Int Ed* 57(1):102–120
- Li J, Zhang Y, Li L, Wang Y, Zhang L, Zhang B, Wang F (2020) Formation of dumbbell and sphere-like CuO as high-performance anode materials for lithium-ion batteries. *Mater Lett* 261:127058
- Wang C, Zhao Y, Su D, Ding C, Wang L, Yan D, Jin H (2017) Synthesis of NiO nano octahedron aggregates as high-performance anode materials for lithium-ion batteries. *Electrochim Acta* 231:272–278
- Jiang T, Bu F, Feng X, Shakir I, Hao G, Xu Y (2017) Porous Fe_2O_3 nanoframeworks encapsulated within three-dimensional graphene as high-performance flexible anode for lithium-ion battery. *ACS Nano* 11(5):5140–5147
- Zhang C, Liu S, Qi Y, Cui F, Yang X (2018) Conformal carbon coated TiO_2 aerogel as superior anode for lithium-ion batteries. *Chem Eng J* 351:825–831
- Bhattacharya P, Lee J, Kar K, Park H (2019) Carambola-shaped SnO_2 wrapped in carbon nanotube network for high volumetric capacity and improved rate and cycle stability of lithium-ion battery. *Chem Eng J* 369:422–431

15. Hu R, Zhang H, Bu Y, Zhang H, Zhao B, Yang C (2017) Porous Co_3O_4 nanofibers surface-modified by reduced graphene oxide as a durable, high-rate anode for lithium-ion battery. *Electrochim Acta* 228:241–250
16. Yang Y, Yuan W, Zhang X, Wang C, Yuan Y, Huang Y, Tang Y (2020) A review on Fe_xO_y -based materials for advanced lithium-ion batteries. *Renew Sust Energ Rev* 127:109884
17. Zeng Z, Zhao H, Wang J, Lv P, Zhang T, Xia Q (2014) Nanostructured Fe_3O_4 @C as anode material for lithium-ion batteries. *J Power Sources* 248:15–21
18. Cheng Y, Chen C, Yang S, Li Y, Peng B, Chang C, Liu C (2018) Freestanding three-dimensional CuO/NiO core-shell nanowire arrays as high-performance lithium-ion battery anode. *Sci Rep* 8(1):18034
19. Saadat S, Zhu J, Sim D, Hng H, Yazami R, Yan Q (2013) Coaxial Fe_3O_4 /CuO hybrid nanowires as ultra-fast charge/discharge lithium-ion battery anodes. *J Mater Chem A* 1(30):8672–8678
20. Li M, Wang Y, Yang C, Jiang Q (2018) In situ grown Co_3O_4 nanocubes on N-doped graphene as a synergistic hybrid for applications in nickel metal hydride batteries. *Int J Hydrog Energy* 43(39):18421–18435
21. De B, Banerjee S, Verma K, Pal T, Manna P, Kar K (2020) Transition metal oxides as electrode materials for supercapacitors. *Handbook of nanocomposite supercapacitor materials II* (pp. 89–111). Springer, Cham
22. Cui X, Song B, Cheng S, Xie Y, Shao Y, Sun Y (2017) Synthesis of carbon nanotube (CNT)-entangled CuO nanotube networks via CNT-catalytic growth and in situ thermal oxidation as additive-free anodes for lithium-ion batteries. *Nanotechnology* 29(3):035603
23. Lin X, Zhang J, Tong X, Li H, Pan X, Ning P, Li Q (2017) Templating synthesis of Fe_2O_3 hollow spheres modified with Ag nanoparticles as superior anode for lithium-ion batteries. *Sci Rep* 7(1):1–9
24. Peng P, Zhao Q, Zhu P, Liu W, Yuan Y, Ding R, Liu E (2021) Amorphous Fe_2O_3 film-coated mesoporous Fe_2O_3 core-shell nanosphere prepared by quenching as a high-performance anode material for lithium-ion batteries. *J Electroanal Chem* 898:115633
25. Zhang Y, Zhang K, Ren S, Jia K, Dang Y, Liu G, Qiu J (2019) 3D nanoflower-like composite anode of $\alpha\text{-Fe}_2\text{O}_3$ /coal-based graphene for lithium-ion batteries. *J Alloys Compd* 792:828–834
26. Ren Y, Zhang S, Zhang L, He X (2020) 3D Si@Cu-Ni nanopillars array composite as carbon/binder free anode for lithium-ion battery. *J Mater Res Technol* 9(2):1549–1558
27. Sun M, Sun M, Yang H, Song W, Nie Y, Sun S (2017) Porous Fe_2O_3 nanotubes as advanced anode for high performance lithium-ion batteries. *Ceram Int* 43(1):363–367
28. Zhang Y, Ma Q, Wang S, Liu X, Li L (2018) Poly (vinyl alcohol)-assisted fabrication of hollow carbon spheres/reduced graphene oxide nanocomposites for high-performance lithium-ion battery anodes. *ACS Nano* 12(5):4824–4834
29. Huang J, Wang W, Lin X, Gu C, Liu J (2018) Three-dimensional sandwich-structured NiMn_2O_4 @reduced graphene oxide nanocomposites for highly reversible Li-ion battery anodes. *J Power Sources* 378:677–684
30. Wang Y, Wang L, Ma Z, Gao L, Yin X, Song A, Gao W (2018) 3D-structured carbon-coated MnO/graphene nanocomposites with exceptional electrochemical performance for Li-ion battery anodes. *J Solid State Electrochem* 22(10):2977–2987
31. Wang G, Bi X, Yue H, Jin R, Wang Q, Gao S, Lu J (2019) Sacrificial template synthesis of hollow C@ MoS_2 @PPy nanocomposites as anodes for enhanced sodium storage performance. *Nano Energy* 60:362–370
32. Li Z, Xie G, Wang C, Liu Z, Chen J, Zhong S (2021) Binder free $\text{Cu}_2\text{O}/\text{CuO}/\text{Cu}/\text{Carbon}$ -polymer composite fibers derived from metal/organic hybrid materials through electrodeposition method as high performance anode materials for lithium-ion batteries. *J Alloys Compd* 864:158585
33. Liu R, Zhang C, Wang Q, Shen C, Wang Y, Dong Y, Wu M (2018) Facile synthesis of $\alpha\text{-Fe}_2\text{O}_3$ @C hollow spheres as ultra-long cycle performance anode materials for lithium-ion battery. *J Alloys Compd* 742:490–496
34. Chen Q, Heng B, Wang H, Sun D, Wang B, Sun M, Tang Y (2015) Controlled facile synthesis of hierarchical CuO/MnO_2 core-shell nanosheet arrays for high-performance lithium-ion battery. *J Alloys Compd* 641:80–86
35. Balandin A, Ghosh S, Bao W, Calizo I, Teweldebrhan D, Miao F, Lau C (2008) Superior thermal conductivity of single-layer graphene. *Nano Lett* 8(3):902–907
36. Yoo E, Kim J, Hosono E, Zhou HS, Kudo T, Honma I (2008) Large reversible Li storage of graphene nanosheet families for use in rechargeable lithium-ion batteries. *Nano Lett* 8(8):2277–2282
37. Marcano D, Kosynkin D, Berlin J, Sinitiskii A, Sun Z, Slesarev A, Tour J (2010) Improved synthesis of graphene oxide. *ACS Nano* 4(8):4806–4814
38. Ranjbar-Azad M, Behpour M (2021) Facile in situ co-precipitation synthesis of $\text{CuO-NiO}/\text{rGO}$ nanocomposite for lithium-ion battery anodes. *J Mater Sci Mater Electron* 1–14
39. Jamatia R, Gupta A, Dam B, Saha M, Pal A (2017) Graphite oxide: a metal free highly efficient carbocatalyst for the synthesis of 1, 5-benzodiazepines under room temperature and solvent free heating conditions. *Green Chem* 19(6):1576–1585
40. Stankovich S, Dikin D, Piner R, Kohlhaas K, Kleinhammes A, Jia Y, Ruoff R (2007) Synthesis of graphene-based nanosheets via chemical reduction of exfoliated graphite oxide. *Carbon* 45(7):1558–1565
41. Pastrana E, Zamora V, Wang D, Alarcón H (2019) Fabrication and characterization of $\alpha\text{-Fe}_2\text{O}_3/\text{CuO}$ heterostructure thin films via dip-coating technique for improved photoelectrochemical performance. *Adv Nat Sci: Nanosci Nanotechnol* 10(3):035012
42. Zhang Y, Li J, Gong Z, Xie J, Lu T, Pan L (2021) Nitrogen and sulfur co-doped vanadium carbide MXene for highly reversible lithium-ion storage. *J Colloid Interface Sci* 587:489–498
43. Li J, Ding Z, Li J, Wang C, Pan L, Wang G (2021) Synergistic coupling of NiS_{1.03} nanoparticle with S-doped reduced graphene oxide for enhanced lithium and sodium storage. *Chem Eng J* 407:127199
44. Deng Z, Ma Z, Li Y, Li Y, Chen L, Yang X, Su B (2018) Boosting lithium-ion storage capability in CuO nanosheets via synergistic engineering of defects and pores. *Front Chem* 6:428
45. Liu X, Si W, Zhang J, Sun X, Deng J, Baunack S, Schmidt O (2014) Free-standing Fe_2O_3 nanomembranes enabling ultra-long cycling life and high-rate capability for Li-ion batteries. *Sci Rep* 4(1):1–8
46. Di Lecce D, Verrelli R, Campanella D, Marangon V, Hassoun J (2017) A new $\text{CuO-Fe}_2\text{O}_3$ -mesocarbon microbeads conversion anode in a high-performance lithium-ion battery with a $\text{Li}_{1.35}\text{Ni}_{0.48}\text{Fe}_{0.1}\text{Mn}_{1.72}\text{O}_4$ spinel cathode. *ChemSusChem* 10(7):1607–1615
47. Abbas S, Hussain S, Ali S, Ahmad N, Ali N, Abbas S, Ali Z (2013) Modification of carbon nanotubes by CuO-doped NiO nanocomposite for use as an anode material for lithium-ion batteries. *J Solid State Chem* 202:43–50
48. Liu H, Wang X, Wang J, Xu H, Yu W, Dong X, Wang L (2017) High electrochemical performance of nanoporous $\text{Fe}_3\text{O}_4/\text{CuO}/\text{Cu}$ composites synthesized by dealloying Al-Cu-Fe quasicrystal. *J Alloys Compd* 729:360–369
49. Wang G, Liu T, Luo Y, Zhao Y, Ren Z, Bai J, Wang H (2011) Preparation of Fe_2O_3 /graphene composite and its electrochemical performance as an anode material for lithium-ion batteries. *J Alloys Compd* 509(24):L216–L220

50. Xiao L, Wu D, Han S, Huang Y, Li S, He M, Feng X (2013) Self-assembled Fe_2O_3 /graphene aerogel with high lithium storage performance. *ACS Appl Mater Interfaces* 5(9):3764–3769
51. Zhu X, Zhu Y, Murali S, Stoller M, Ruoff RS (2011) Nanostructured reduced graphene oxide/ Fe_2O_3 composite as a high-performance anode material for lithium-ion batteries. *ACS Nano* 5(4):3333–3338
52. Liu H, Luo SH, Hu DB, Liu X, Wang Q, Wang ZY, Hao AM (2019) Design and synthesis of carbon-coated $\alpha\text{-Fe}_2\text{O}_3@ \text{Fe}_3\text{O}_4$ heterostructured as anode materials for lithium-ion batteries. *Appl Surf Sci* 495:143590
53. Xue Z, Li L, Cao L, Zheng W, Yang W, Yu X (2020) A simple method to fabricate $\text{NiFe}_2\text{O}_4/\text{NiO}@ \text{Fe}_2\text{O}_3$ core-shelled nanocubes based on Prussian blue analogues for lithium-ion battery. *J Alloys Compd* 825:153966
54. (2016) Active Fe_2O_3 nanoparticles encapsulated in porous gC_3N_4 /graphene sandwich-type nanosheets as superior anode for high-performance lithium-ion batteries
55. Li M, Du H, Kuai L, Huang K, Xia Y, Geng B (2017) Scalable dry production process of a superior 3D net-like carbon-based iron oxide anode material for lithium-ion batteries. *Angew Chem Int Ed* 56(41):12649–12653
56. Wan L, Tang Y, Chen L, Wang K, Zhang J, Gao Y, Pan L (2021) In-situ construction of $\text{g-C}_3\text{N}_4/\text{Mo}_2\text{CT}_x$ hybrid for superior lithium storage with significantly improved Coulombic efficiency and cycling stability. *Chem Eng J* 410:128349

Publisher's Note Springer Nature remains neutral with regard to jurisdictional claims in published maps and institutional affiliations.

Springer Nature or its licensor holds exclusive rights to this article under a publishing agreement with the author(s) or other rightsholder(s); author self-archiving of the accepted manuscript version of this article is solely governed by the terms of such publishing agreement and applicable law.